Optical excitations with even symmetry in insulating cuprates

2000 J. Phys.: Condens. Matter 12 8847

(http://iopscience.iop.org/0953-8984/12/41/311)

J. Phys.: Condens. Matter **12** (2000) 8847–8862. Printed in the UK PII: S0953-8984(00)14757-5

Optical excitations with even symmetry in insulating cuprates

Eiichi Hanamura†, Nguyen Trung Dan‡§ and Yukito Tanabe‖

† Chitose Institute of Science and Technology, 785-65 Bibi, Chitose-City, Hokkaido 066-8655, Japan
‡ Optical Sciences Center, University of Arizona, Tucson, AZ 85721, USA
§ ERATO Cooperative Excitation Project, Japan Science and Technology Corporation
‖ Department of Applied Physics, University of Tokyo, 7-3-1 Hongo, Bunkyo-ku, Tokyo 113, Japan

Received 15 June 2000, in final form 31 August 2000

Abstract. An excitonic cluster model, which can take into account both the strong correlation effect of 3d electrons and the itinerant nature of electronic excitations, and consequently both the bound and unbound states of electrons and holes on the same footing, is applied to describe optical excitations with even symmetry in insulating cuprates, i.e. parent crystals of high-temperature superconductors. These states are observable in large-shift Raman scattering and two-photon absorption spectra.

1. Introduction

Competitive behaviour between the strong correlation of 3d electrons and the itinerant property of doped holes in transition-metal oxides of perovskite structure induces a rich variety of transport phenomena such as high-temperature superconductors in cuprates [1] and colossal negative magneto-resistance in manganites [2]. Even in the non-doped crystals which are antiferromagnetic insulators, nonlinear as well as linear optical responses have been studied experimentally [3–25]. Theoretical understanding, however, is still controversial because of the difficulty of describing the competitive behaviours between the strong correlation effect of 3d electrons on Cu ions and the itinerant property of the particles and holes involved. To describe these optical responses, we have proposed the excitonic cluster model [26] by taking into account both the strong correlation effect of 3d electrons and the itinerant nature of electronic excitations. Consequently both the electron–hole bound and unbound states can be described on the same footing. Note that the effective transfer matrix elements t_0 between the transition-metal 3d and the oxygen 2p orbitals, and the elements t_p between the neighbouring oxygen 2p orbitals, and the binding energy V of the charge-transfer (CT) exciton are all of the same order of magnitude for many perovskite-type cuprates. On the other hand, the correlation energy U of 3d electrons and the energy separation $|E_d - E_p|$ between the $O(2p_\sigma)$ and $Cu(3d_{x^2-y^2})$ are much larger than those values of t_0, t_p and V [26–31]. The excitonic cluster model is formulated by making the best use of this situation [26, 32].

The excitonic cluster model was applied first to the dipole-allowed states with E_u symmetry of the D_{4h} representation [32], because the linear absorption spectrum and the resonance-enhancement spectrum of two-magnon Raman scattering (RS) are described in terms of E_u modes. As a result, the detailed structures of these spectra were found to depend sensitively on the values of t_0, t_p and V, although the essential spectra are determined by CuO_2 planes.

0953-8984/00/418847+16$30.00

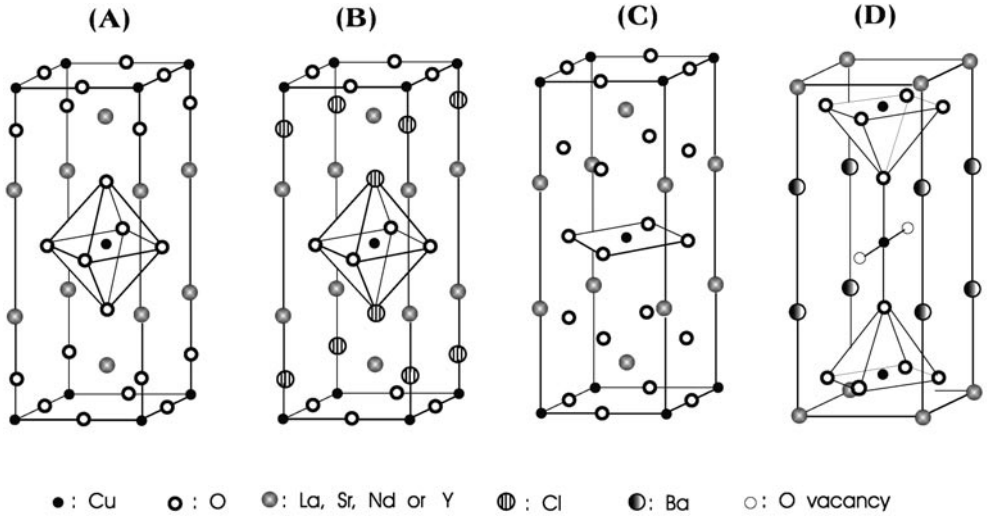

Figure 1. Crystal structures of: (A) La_2CuO_4, (B) $Sr_2CuO_2Cl_2$, (C) Nd_2CuO_4 and (D) $YBa_2Cu_3O_6$.

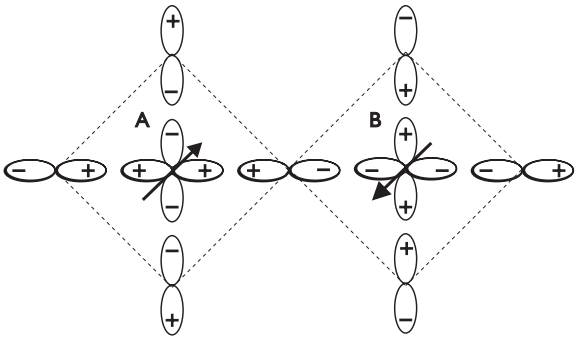

Figure 2. Schematic diagram of the hybridization of the O $2p_{x,y}$ and Cu $3d_{x^2-y^2}$ orbitals. The + and − signs represent the phase of wavefunctions of O $2p_{x,y}$ orbitals around Cu $3d_{x^2-y^2}$ orbitals in A- and B-sublattices.

We could also understand the material dependence of these values, e.g. the dependence on the crystal structures such as shown in figure 1. In the present paper, we apply the excitonic cluster model to the even-symmetry modes in the visible wavelength region, which are observed by the nonlinear optical responses. First we will be able to remove the inconsistencies in assignment of the observed signals on the large-shift RS spectra and second to give the correct assignment on the two-photon absorption (TPA) spectrum of the insulating AF cuprates of perovskite-type.

In section 2, basis functions of even modes symmetry adapted to the D_{4h} representation are derived for the three-band Mott–Hubbard Hamiltonian. An energy matrix is calculated with these even-symmetry functions as bases and is diagonalized for the TPA-active and RS-active A_{1g}, B_{1g}, A_{2g} and B_{2g} modes in section 3. Some characteristics of large-shift RS and TPA spectra due to these modes are derived in section 4. We compare in section 5 the present results obtained in sections 3 and 4 with the observed spectra and discuss some remaining discrepancies.

2. Hamiltonian and even-symmetry states

We discuss in the present paper the even-symmetry states of cuprates: (a) La_2CuO_4; (b) $Sr_2CuO_2Cl_2$; (c) Nd_2CuO_4; and (d) $YBa_2Cu_3O_6$. These have perovskite structures but the types are different as shown in figure 1. These differences result in delicate differences in the optical spectra through the different relative magnitudes of t_0, t_p and V as discussed in [26, 32]. However, the basic spectra look similar as the low-lying optical excitation of these crystals in the visible region is determined in common by the CuO_2 plane. The relevant orbitals, i.e. Cu($3d_{x^2-y^2}$), of A- and B-sublattices in the AF structure and O($2p_\sigma = 2p_{x,y}$) surrounding these are drawn in figure 2 together with the phases of these wavefunctions chosen in this paper. We will use the same three-band Mott–Hubbard Hamiltonian as in [26, 32]: the O $2p_\sigma$ band ($p_{l\sigma}$, $p^\dagger_{l\sigma}$) with its central energy $E_p + U_p$, singly and doubly occupied Cu $3d_{x^2-y^2}$ bands ($d_{i\sigma}$, $d^\dagger_{i\sigma}$) with E_d and $E_d + U$ as central energies, respectively. This system has D_{4h} symmetry and is described in the site-representation basis as

$$H_{el} = \sum_{i,\sigma} E_d d^\dagger_{i\sigma} d_{i\sigma} + \sum_{l,\sigma} E_p p^\dagger_{l\sigma} p_{l\sigma} + H'_{el} + U \sum_i d^\dagger_{i\uparrow} d_{i\uparrow} d^\dagger_{i\downarrow} d_{i\downarrow} + U_p \sum_l p^\dagger_{l\uparrow} p_{l\uparrow} p^\dagger_{l\downarrow} p_{l\downarrow} + V \sum_{i\sigma\sigma'} \sum_{l\in\{i\}} d^\dagger_{i\sigma} d_{i\sigma} p^\dagger_{l\sigma'} p_{l\sigma'} \tag{1}$$

$$H'_{el} = t_0 \sum_{i\sigma} \sum_{l\in\{i\}} d^\dagger_{i\sigma} p_{l\sigma} + t_p \sum_{l\sigma} \sum_{l'\in\{l\}} p^\dagger_{l\sigma} p_{l'\sigma}. \tag{2}$$

Here U and U_p are the on-site Coulomb repulsion at the Cu and O sites, respectively, and V is the nearest-neighbour Cu–O interatomic Coulomb repulsion. The first and second terms of H'_{el} (2) bring in, respectively, the hybridization between the nearest-neighbour Cu and O orbitals ($l \in \{i\}$ in equation (2)), and that between the two nearest-neighbour oxygen orbitals ($l' \in \{l\}$ in equation (2)). Note that our non-relativistic Hamiltonian (1) and (2) with D_{4h} symmetry does not contain: (a) spin–orbit interaction; (b) magnetic anisotropy energy which determines the spin direction; and (c) magnetic dipole–dipole interaction. Therefore, only the relative spin configuration is determined by (d) the Heisenberg–Dirac exchange interaction, while the absolute direction of the spin relative to the crystal axis cannot be fixed by the exchange interaction itself. In the ordered phase of the real crystal, the spin configuration is determined by the combined effect of processes (a), (b), (c) and (d). Therefore, it would be natural to use the observed magnetic group in describing the response of the crystals. Even when the crystal suffers the structure change into the orthorhombic phase and/or the AF phase transition, the Hamiltonian with D_{4h} symmetry gives a good starting point as will be discussed in section 5. The electronic ground state of this Hamiltonian has one electron ($3d_{x^2-y^2}$) per Cu^{2+} ion and has fully occupied 2p electrons per O^{2-} ion surrounding this Cu^{2+} ion. The ground state $|g\rangle$ is represented in the site representation as follows:

$$|g\rangle \equiv \prod_{m+n=\text{even}}^{A} d^\dagger_\uparrow(2m, 2n) \prod_{m+n=\text{odd}}^{B} d^\dagger_\downarrow(2m, 2n) \prod_{m+n=\text{odd}} p^\dagger_\uparrow(m, n)\, p^\dagger_\downarrow(m, n)\, |0\rangle \tag{3}$$

where the vacuum $|0\rangle$ is defined by the product of whole $O(2p)^4$ and $Cu(3d)^8$ in which two $2p_\sigma$ electrons and two $3d_{x^2-y^2}$ electrons are missing, respectively. This AF ground state can be accepted for two-dimensional systems as this was well confirmed experimentally [33] and the quantum fluctuation could be described by the spin-wave excitations as [12–14] have shown. For one-dimensional systems, however, the quantum fluctuation is known to be so large that we confine ourselves to the two-dimensional systems in the present paper.

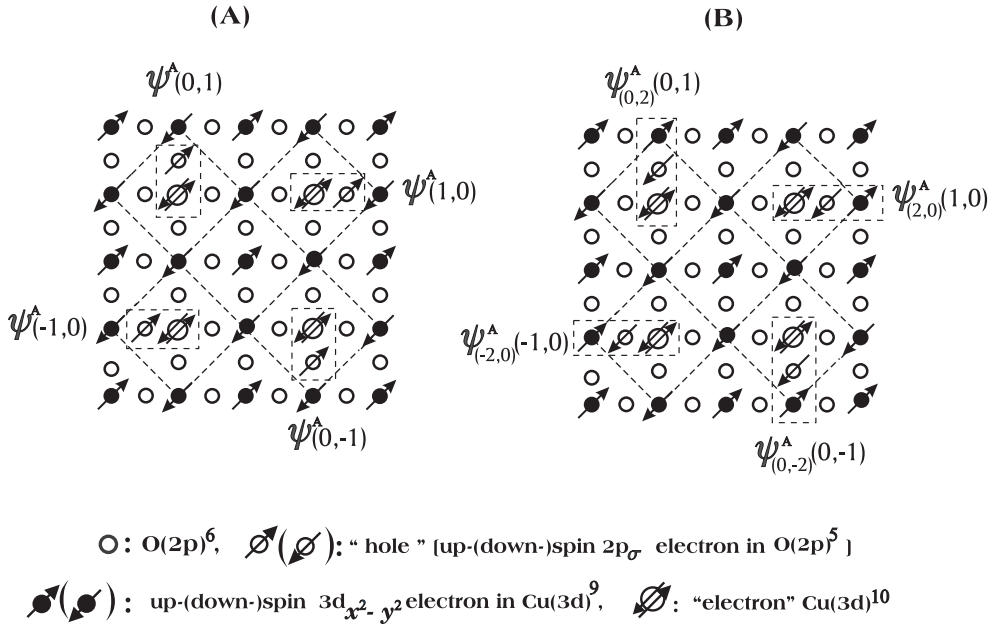

Figure 3. (A) Charge-transfer excitation $\psi^A(1,0)$ in which a down-spin electron in the $2p_x$ orbital of the $O^{2-}(1,0)$ ion is transferred to the A-sublattice Cu ion, and (B) $\psi^A_{(2,0)}(1,0)$ in which two electrons, i.e. an up-spin electron in $O^-(1,0)$ $2p_x$ and a down-spin $3d_{x^2-y^2}$ electron on the nearest-neighbour Cu(2, 0) ion of the B-sublattice are exchanged. Equivalent excitations under D_{4h} symmetry are also drawn in both (A) and (B).

The radiation field can induce the CT excitations through the transition dipole moment which is linearly proportional to t_0 and also to the unit vector drawn from the ith lattice point to the lth one. The CT excitation $\psi^A(1,0) = d^\dagger_{A\downarrow}(0,0)p_{x\downarrow}(1,0)|g\rangle$ represents the formation of a bound CT exciton with the 'electron' $(3d_{x^2-y^2})^2$ at the A-sublattice Cu $(0,0)$ and the 'hole' $(2p)^5$ at O $(1,0)$ as shown in figure 3(A). When two electrons of $O(2p_x\uparrow)$ at $(1,0)$ and $Cu(3d_{x^2-y^2}\downarrow)$ at the B-sublattice $(2,0)$ are exchanged through the second-order process in t_0, the state $\psi^A_{(2,0)}(1,0) = d^\dagger_{A\downarrow}(0,0)p_{x\uparrow}(1,0)d^\dagger_{B\uparrow}(2,0)d_{B\downarrow}(2,0)|g\rangle$ is created as shown in figure 3(B). Here the argument $(1,0)$ of $\psi^A_{(2,0)}(1,0)$ also describes the location of the 'hole' O^- (now with its down spin) and the suffix $(2,0)$ gives that of the reversed Cu^{2+} spin in the B-sublattice.

Reflecting the D_{4h} symmetry of the CuO_2 plane, we have four equivalent CT excitations: $\psi^{A(B)}(1,0)$, $\psi^{A(B)}(0,1)$, $\psi^{A(B)}(-1,0)$ and $\psi^{A(B)}(0,-1)$ around the A-(B-)sublattice Cu ions, corresponding to the four diagrams in figure 3(A). Four dipole-allowed states around the A-sublattice are mixed with each other by the second-order process in t_0, i.e. $t_1 = t_0^2/(U - U_p - E_p - V)$ and t_p. When we diagonalize the energy matrix,

$$\begin{pmatrix} E_0 & t_1+t_p & t_1 & t_1+t_p \\ t_1+t_p & E_0 & t_1+t_p & t_1 \\ t_1 & t_1+t_p & E_0 & t_1+t_p \\ t_1+t_p & t_1 & t_1+t_p & E_0 \end{pmatrix} \begin{pmatrix} \psi^A(1,0) \\ \psi^A(0,1) \\ \psi^A(-1,0) \\ \psi^A(0,-1) \end{pmatrix} = E \begin{pmatrix} \psi^A(1,0) \\ \psi^A(0,1) \\ \psi^A(-1,0) \\ \psi^A(0,-1) \end{pmatrix} \tag{4}$$

we obtain the eigenfunctions and eigenenergies of the four CT states

$$\Psi^1_{aA} = \frac{1}{2}\{\psi^A(1,0) + \psi^A(0,1) + \psi^A(-1,0) + \psi^A(0,-1)\} \qquad E_0 + 3t_1 + 2t_p$$

$$\Psi^1_{bA} = \frac{1}{2}\{\psi^A(1,0) - \psi^A(0,1) + \psi^A(-1,0) - \psi^A(0,-1)\} \qquad E_0 - t_1 - 2t_p$$
$$\Psi^1_{exA} = \frac{1}{\sqrt{2}}\{\psi^A(1,0) - \psi^A(-1,0)\} \qquad E_0 - t_1$$
$$\Psi^1_{eyA} = \frac{1}{\sqrt{2}}\{\psi^A(0,1) - \psi^A(0,-1)\} \qquad E_0 - t_1. \tag{5}$$

Here the diagonal energy E_0 is evaluated to the fourth order in t_0, i.e. to the order of J the superexchange energy which induces the AF structure, in addition to the exchange energy to the second order in t_0

$$E_0 \equiv U - E_p - U_p - V + t_1 - t_1' - t_2' + J \tag{6}$$

where

$$t_1' = \frac{t_0^2}{U - E_p - U_p - 2V} \tag{7}$$
$$t_2 = \frac{t_0^2}{E_p + U_p} \qquad t_2' = \frac{t_0^2}{E_p + U_p + V} \tag{8}$$

and

$$J = \frac{4t_0^4}{(U - E_p - U_p - V)^2}\left[\frac{1}{U} + \frac{1}{2(U - E_p - U_p - 2V)}\right]. \tag{9}$$

Thus we have four states $A_{1g}(\Psi^1_{aA})$, $B_{1g}(\Psi^1_{bA})$, and two-fold degenerate E_u (Ψ^1_{exA} and Ψ^1_{eyA}) around the A-sublattice, that are symmetry-adapted according to the irreducible representations of the group D_{4h}. In the paramagnetic phase with the symmetry D_{4h}, the charge distribution $\Psi^*_g\Psi_g$ has A_{1g} symmetry of the point group D_{4h}. The symmetry of the excited states in (5), which is judged by that of its product with the ground state Ψ^*_g, or the symmetry of excitons [32], is A_{1g}, B_{1g} and two-fold degenerate E_u of the paramagnetic group D_{4h}, in this order. Note here that the symmetry operator R affects only the orbital part of the product, e.g. $\Psi^*_g\Psi^1_{aA}$, without rotating the spin vector of magnetic ions. We also have similar expressions for the eigenfunctions and eigenenergies around the B-sublattice. Only the states with $E_u^{x,y}$ symmetry (Ψ^1_{exA} and Ψ^1_{eyA}) can contribute to the absorption and two-magnon RS. The states $A_{1g}(\Psi^1_{aA})$ and $B_{1g}(\Psi^1_{bA})$ are observable in the TPA spectrum and in the large-shift RS in which the incident light frequency ω is much larger than the excitation energy $E(B_{1g})$ and $E(A_{1g})$.

Only the states with the same symmetry in the site representation are intermixed with each other through H'_{el} (2). The states $\Psi^m_{eEA}(n)$ were used as the bases to describe the linear and two-magnon Raman scattering. Here the superscript m denotes the distance between the 'electron' at the origin and the 'hole', while the argument n stands for the separation between the reversed spin and the 'hole', and the argument (0) represents the case of the nearest neighbour and no argument indicates the case without reserved spin. We derive the basis function with A_{1g} and B_{1g} symmetry of the order of t_0 in the same way as for $\Psi^m_{eEA}(n)$. The same second-order exchanges t_1 and t_2 described above induce the states $\Psi^1_{aA}(0)$ and $\Psi^1_{bA}(0)$ shown in figure 3(B)

$$\Psi^1_{aA}(0) = \tfrac{1}{2}\{\psi^A_{(2,0)}(1,0) + \psi^A_{(0,2)}(0,1) + \psi^A_{(-2,0)}(-1,0) + \psi^A_{(0,-2)}(0,-1)\} \tag{10}$$
$$\Psi^1_{bA}(0) = \tfrac{1}{2}\{\psi^A_{(2,0)}(1,0) - \psi^A_{(0,2)}(0,1) + \psi^A_{(-2,0)}(-1,0) - \psi^A_{(0,-2)}(0,-1)\}. \tag{11}$$

When the 'hole' propagates to the second- and third-neighbour oxygens measured from the doubly occupied Cu, the 'electron' at the $(0,0)$ site, the following A_{1g} and B_{1g} states are

derived after applying two steps of CT t_0 on Ψ^1_{aA} and Ψ^1_{bA}, respectively†,

$$\Psi^2_{aA} = \frac{1}{2\sqrt{2}}\{\psi^A(2,1) + \psi^A(1,2) + \psi^A(-1,2) + \psi^A(-2,1) + \psi^A(-2,-1) + \psi^A(-1,-2) + \psi^A(1,-2) + \psi^A(2,-1)\} \tag{12}$$

$$\Psi^2_{bA} = \frac{1}{2\sqrt{2}}\{\psi^A(2,1) - \psi^A(1,2) - \psi^A(-1,2) + \psi^A(-2,1) + \psi^A(-2,-1) - \psi^A(-1,-2) - \psi^A(1,-2) + \psi^A(2,-1)\} \tag{13}$$

$$\Psi^3_{aA} = \frac{1}{2}\{\psi^A(3,0) + \psi^A(0,3) + \psi^A(-3,0) + \psi^A(0,-3)\} \tag{14}$$

$$\Psi^3_{bA} = \frac{1}{2}\{\psi^A(3,0) - \psi^A(0,3) + \psi^A(-3,0) - \psi^A(0,-3)\}. \tag{15}$$

These states are of the same order in t_0 as $\Psi^1_{aA}(0)$ and $\Psi^1_{bA}(0)$. To the next higher order in t_0, i.e. in t_0^4, we must include the following states with the 'electron' and 'hole' still in the nearest neighbour but with the 'hole' [$O(2p_\sigma\downarrow)$] and the reserved spin (the magnon) propagating away from the original locations given in the states $\Psi^1_{aA}(0)$ and $\Psi^1_{bA}(0)$:

$$\Psi^1_{aA}(2) = \frac{1}{2}\{\psi^A_{(2,0)}(-1,0) + \psi^A_{(0,2)}(0,-1) + \psi^A_{(-2,0)}(1,0) + \psi^A_{(0,-2)}(0,1)\} \tag{16}$$

$$\Psi^1_{bA}(2) = \frac{1}{2}\{\psi^A_{(2,0)}(-1,0) - \psi^A_{(0,2)}(0,-1) + \psi^A_{(-2,0)}(1,0) - \psi^A_{(0,-2)}(0,1)\} \tag{17}$$

$$\Psi^1_{aA}(1) = \frac{1}{2\sqrt{2}}\{\psi^A_{(2,0)}(0,1) + \psi^A_{(0,2)}(-1,0) + \psi^A_{(-2,0)}(0,-1) + \psi^A_{(0,-2)}(1,0) + \psi^A_{(2,0)}(0,-1) + \psi^A_{(0,2)}(1,0) + \psi^A_{(-2,0)}(0,1) + \psi^A_{(0,-2)}(-1,0)\} \tag{18}$$

$$\Psi^1_{bA}(1) = \frac{1}{2\sqrt{2}}\{\psi^A_{(2,0)}(0,1) - \psi^A_{(0,2)}(-1,0) + \psi^A_{(-2,0)}(0,-1) - \psi^A_{(0,-2)}(1,0) + \psi^A_{(2,0)}(0,-1) - \psi^A_{(0,2)}(1,0) + \psi^A_{(-2,0)}(0,1) - \psi^A_{(0,-2)}(-1,0)\}. \tag{19}$$

The last set of basis functions, in the fourth order of t_0, contains A_{2g} and B_{2g} representations in D_{4h} symmetry and is expressed as

$$\Psi^1_{a'A}(1) = \frac{1}{2\sqrt{2}}\{\psi^A_{(2,0)}(0,1) + \psi^A_{(0,2)}(-1,0) + \psi^A_{(-2,0)}(0,-1) + \psi^A_{(0,-2)}(1,0) - \psi^A_{(2,0)}(0,-1) - \psi^A_{(0,2)}(1,0) - \psi^A_{(-2,0)}(0,1) - \psi^A_{(0,-2)}(-1,0)\} \tag{20}$$

$$\Psi^1_{b'A}(1) = \frac{1}{2\sqrt{2}}\{\psi^A_{(2,0)}(0,1) - \psi^A_{(0,2)}(-1,0) + \psi^A_{(-2,0)}(0,-1) - \psi^A_{(0,-2)}(1,0) - \psi^A_{(2,0)}(0,-1) + \psi^A_{(0,2)}(1,9) - \psi^A_{(-2,0)}(0,1) + \psi^A_{(0,-2)}(-1,0)\}. \tag{21}$$

Here a' and b' correspond to A_{2g} and B_{2g}, respectively.

When we exchange the 'hole' $O(2p)^5$ ($2p_x\uparrow$ electron) in Ψ^2_{aA} and Ψ^3_{aA} and the $3d_{x^2-y^2}\downarrow$ electron on the nearest-neighbour $Cu(3d)^9$ in the B-sublattice, we have the following states which are the same order in t_0 as $\Psi^1_{aA}(2)$, $\Psi^1_{aA}(1)$ and $\Psi^1_{a'A}(1)$, i.e. by t_0^4 higher than ψ^1_{aA} and Ψ^1_{bA}:

$$\Psi^2_{aA}(0) = \frac{1}{2\sqrt{2}}\{\psi^A_{(2,0)}(2,1) + \psi^A_{(0,2)}(1,2) + \psi^A_{(0,2)}(-1,2) + \psi^A_{(-2,0)}(-2,1) + \psi^A_{(-2,0)}(-2,-1) + \psi^A_{(0,-2)}(-1,-2) + \psi^A_{(0,-2)}(1,-2) + \psi^A_{(2,0)}(2,-1)\} \tag{22}$$

† See, for example, [34] for the methods of making the symmetry-adapted basis functions.

$$\Psi^2_{bA}(0) = \frac{1}{2\sqrt{2}}\{\psi^A_{(2,0)}(2,1) - \psi^A_{(0,2)}(1,2) - \psi^A_{(0,2)}(-1,2) + \psi^A_{(-2,0)}(-2,1) + \psi^A_{(-2,0)}(-2,-1) - \psi^A_{(0,-2)}(-1,-2) - \psi^A_{(0,-2)}(1,-2) + \psi^A_{(2,0)}(2,-1)\} \quad (23)$$

$$\Psi^3_{aA}(0) = \frac{1}{2}\{\psi^A_{(2,0)}(3,0) + \psi^A_{(0,2)}(0,3) + \psi^A_{(-2,0)}(-3,0) + \psi^A_{(0,-2)}(0,-3)\} \quad (24)$$

$$\Psi^3_{bA}(0) = \frac{1}{2}\{\psi^A_{(2,0)}(3,0) - \psi^A_{(0,2)}(0,3) + \psi^A_{(-2,0)}(-3,0) - \psi^A_{(0,-2)}(0,-3)\}. \quad (25)$$

To this order, we must also include the following three sets of states:

$$\Psi^4_{aA} = \frac{1}{2\sqrt{2}}\{\psi^A(3,2) + \psi^A(2,3) + \psi^A(-2,3) + \psi^A(-3,2) + \psi^A(-3,-2) + \psi^A(-2,-3) + \psi^A(2,-3) + \psi^A(3,-2)\} \quad (26)$$

$$\Psi^4_{bA} = \frac{1}{2\sqrt{2}}\{\psi^A(3,2) - \psi^A(2,3) - \psi^A(-2,3) + \psi^A(-3,2) + \psi^A(-3,-2) - \psi^A(-2,-3) - \psi^A(2,-3) + \psi^A(3,-2)\} \quad (27)$$

$$\Psi^5_{aA} = \frac{1}{2\sqrt{2}}\{\psi^A(4,1) + \psi^A(1,4) + \psi^A(-1,4) + \psi^A(-4,1) + \psi^A(-4,-1) + \psi^A(-1,-4) + \psi^A(1,-4) + \psi^A(4,-1)\} \quad (28)$$

$$\Psi^5_{bA} = \frac{1}{2\sqrt{2}}\{\psi^A(4,1) - \psi^A(1,4) - \psi^A(-1,4) + \psi^A(-4,1) + \psi^A(-4,-1) - \psi^A(-1,-4) - \psi^A(1,-4) + \psi^A(4,-1)\} \quad (29)$$

$$\Psi^6_{aA} = \frac{1}{2}\{\psi^A(5,0) + \psi^A(0,5) + \psi^A(-5,0) + \psi^A(0,-5)\} \quad (30)$$

$$\Psi^6_{bA} = \frac{1}{2}\{\psi^A(5,0) - \psi^A(0,5) + \psi^A(-5,0) - \psi^A(0,-5)\}. \quad (31)$$

The basis functions $\Psi^n_{aA}(0)$ and $\Psi^n_{bA}(0)$ ($n = 4, 5, 6$) in which two electrons are exchanged between $[\mathrm{O(2p)}^5, 2\mathrm{p}_\sigma\uparrow]$ and the nearest-neighbour B-sublattice $[\mathrm{Cu(3d)}^9, 3\mathrm{d}_{x^2-y^2}\downarrow]$ are obtained from the above equations and are higher by t_0^6 order than Ψ^1_{aA} and Ψ^1_{bA}.

We repeat these procedures to obtain the corresponding basis functions around the B-sublattice. Only the symmetric state with respect to the interchange of A- and B-sublattices can contribute to the optical responses, that is for $\alpha = a[A_{1g}]$ or $b[B_{1g}]$,

$$\Psi^m_{\alpha+} = \frac{1}{\sqrt{2}}\{\Psi^m_{\alpha A} + \Psi^m_{\alpha B}\} \quad (32)$$

$$\Psi^m_{\alpha+}(n) = \frac{1}{\sqrt{2}}\{\Psi^m_{\alpha A}(n) + \Psi^m_{\alpha B}(n)\}. \quad (33)$$

Then we can finally express the eigenstates belonging to the eigenenergy E_i as a symmetric linear combination of the states (32) and (33) with the same symmetry species:

$$\Psi_{\alpha+}[i] = a_i[\alpha]\Psi^1_{\alpha+} + b_i[\alpha]\Psi^1_{\alpha+}(0) + c_i[\alpha]\Psi^1_{\alpha+}(2) + d_i[\alpha]\Psi^1_{\alpha+}(1) + e_i[\alpha]\Psi^2_{\alpha+} + f_i[\alpha]\Psi^2_{\alpha+}(0) + g_i[\alpha]\Psi^3_{\alpha+} + h_i[\alpha]\Psi^3_{\alpha+}(0) + j_i[\alpha]\Psi^4_{\alpha+} + k_i[\alpha]\Psi^4_{\alpha+}(0) + l_i[\alpha]\Psi^5_{\alpha+} + m_i[\alpha]\Psi^5_{\alpha+}(0) + \cdots. \quad (34)$$

We have considered the excited states symmetry adapted to D_{4h}, taking into account the AF A- and B-sublattices. One may wonder how translational symmetry is taken into consideration in our treatment. Actually, the point group D_{4h} here is to be regarded as the $\boldsymbol{k}$-group (wavevector group) of the space group at the gamma point, because we are concerned

only with the elementary excitations which the visible light can excite. The relation between our treatment and the usual band calculation which neglects the AF structure is simple. Reciprocal-lattice points on the Brillouin-zone boundary in the latter calculation are to be folded on the gamma point of the AF Brillouin zone, so that the separation between the highest and lowest energies in the present calculation will give the observed band width as discussed in [32].

The effect of the translational motion of the exciton as a whole, or the exciton dispersion, however, is not likely to be important as estimated at the end of section 5.

3. Energy matrix and its diagonalization

We derive the secular equation to obtain the eigenenergies $\{E_i\}$ and the corresponding eigenfunctions $\{\psi_{\alpha+}, \alpha = A_{1g} \text{ and } B_{1g}\}$ in terms of the set of basis functions:

$$\{\Psi^1_{\alpha+}, \Psi^1_{\alpha+}(0), \Psi^1_{\alpha+}(2), \Psi^1_{\alpha+}(1), \Psi^2_{\alpha+}, \Psi^2_{\alpha+}(0), \Psi^3_{\alpha+}, \Psi^3_{\alpha+}(0), \Psi^4_{\alpha+}, \Psi^4_{\alpha+}(0), \Psi^5_{\alpha+}, \Psi^5_{\alpha+}(0), \ldots\}. \tag{35}$$

Here the CT effect H'_{el} in (2) is taken into account by the degenerate perturbation method among the basis states (35), and the off-diagonal matrix element is evaluated to first order in t_p and to second order in t_0. Note that all the basis states in (35) are the states of single 'electron' and 'hole' excitations while the intermediate states in evaluating the off-diagonal as well as the diagonal matrices are those of two or zero pair excitations.

The eigenenergies and eigenfunctions of the A_{1g} and B_{1g} modes below 3.0 eV have been found to be independent of the number n of the basis functions as long as $n \geqslant 3$, where n is the 'electron' and 'hole' separation. Therefore we list the secular equation for the case of $n = 3$:

$$M_\alpha \Phi_\alpha = E_\alpha \Phi_\alpha \qquad \alpha = a(A_{1g}) \text{ or } b(B_{1g}) \tag{36}$$

where

$$M_\alpha = \begin{pmatrix} H^\alpha_{I,I} & H^\alpha_{I,II} \\ H^\alpha_{II,I} & H^\alpha_{II,II} \end{pmatrix} \qquad \Phi_\alpha = \begin{pmatrix} a_i[\alpha] \\ b_i[\alpha] \\ c_i[\alpha] \\ \cdots \end{pmatrix}. \tag{37}$$

For the mode $\alpha = a(A_{1g})$,

$$H^a_{I,I} = \begin{pmatrix} \varepsilon^a_0 & -(t'_2 + 2t'_3) & 0 & 0 \\ -(t'_2 + 2t'_3) & \varepsilon'_0 + 2t'_1 - t'_2 - 2t'_3 & 2t_1 - t'_1 & \sqrt{2}(t_p + 2t_1 - t'_1) \\ 0 & 2t_1 - t'_1 & \varepsilon'_0 + t_1 & \sqrt{2}(t_p + t_1) \\ 0 & \sqrt{2}(t_p + 2t_1 - t'_1) & \sqrt{2}(t_p + t_1) & \varepsilon'_0 + t_1 \end{pmatrix} \tag{38}$$

$$H^a_{I,II} = \begin{pmatrix} \sqrt{2}(t_p - \tau) & -\sqrt{2}(\gamma + \tau) & -\tau & -(2\gamma + \tau) \\ -\sqrt{2}(\gamma + \tau) & \sqrt{2}(t_p - \tau) & -(\gamma + \tau) & -\tau \\ 0 & 0 & -\gamma & 0 \\ -\gamma & 0 & 0 & 0 \end{pmatrix} \tag{39}$$

$$H^a_{II,II} = \begin{pmatrix} \varepsilon^a_1 & -(t'_1 + 2t_2 + t_3) & \sqrt{2}(t_p - t_2) & -\sqrt{2}(t'_1 + t_2) \\ -(t'_1 + 2t_2 + t_3) & \varepsilon'_1 - 3t - 2 - 2t_3 & -\sqrt{2}(t'_1 + t_2) & \sqrt{2}(t_p - t_2) \\ \sqrt{2}(t_p - t_2) & -\sqrt{2}(t'_1 + t_2) & \varepsilon_1 - t_2 - t_3 & -(t_2 + t_3) \\ -\sqrt{2}(t'_1 + t_2) & \sqrt{2}(t_p - t_2) & -t_2 - t_3 & \varepsilon'_1 - 2(t_2 + t_3) \end{pmatrix}. \tag{40}$$

For the mode $\alpha = b(B_{1g})$, the [1, 1] component $\varepsilon^a_0 = \varepsilon_0 + 2t_p + 8t_1 - 3t'_1 - t'_2 - 2t'_3$ of equation (38) is replaced by $\varepsilon^b_0 = \varepsilon_0 - 2t_p + t'_1 - t'_2 - 2t'_3$, and the [1, 1] component

Table 1. Material constants (in eV).

	U	U_p	E_p	t_0	t_p	V	J
La_2CuO_4	10.0	3.5	3	0.82	0.40	0.50	0.14
$Sr_2CuO_2Cl_2$	9.76	3.4	3	0.84	0.36	0.42	0.12
Gd_2CuO_4	9.65	3.4	3	0.85	0.30	0.40	0.15
Nd_2CuO_4	9.62	3.4	3	0.85	0.30	0.40	0.13
$YBa_2Cu_3O_6$	10.0	3.4	3	1.0	0.55	0.35	0.12

Table 2. The eigenenergies and eigenvectors of A_{1g} and B_{1g} modes for La_2CuO_4.

$E_i(A_{1g})$ (eV)	a_i	b_i	c_i	d_i	e_i	f_i	g_i	h_i
2.33	0.16	0.58	0.38	−0.54	0.06	−0.06	0.34	0.28
2.63	0.07	0.27	−0.36	0.25	0.67	−0.01	−0.21	0.49
2.68	0.18	−0.15	0.06	0.11	0.20	0.84	0.43	−0.06
3.15	0.33	−0.14	−0.24	0.29	−0.47	−0.19	0.43	0.54
3.43	0.05	−0.56	0.60	−0.08	0.14	0.00	−0.28	0.47
4.00	0.55	0.07	−0.25	−0.33	−0.31	0.33	−0.57	0.05
4.91	0.48	0.31	0.47	0.60	−0.00	−0.11	−0.13	−0.26
5.89	0.55	−0.37	−0.16	−0.27	0.41	−0.37	0.24	−0.31
$E_i(B_{1g})$ (eV)								
1.71	0.85	0.22	0.08	−0.13	−0.05	0.22	0.23	0.32
2.43	0.23	−0.50	−0.43	0.59	0.09	0.36	−0.16	−0.03
2.50	0.11	−0.37	0.18	−0.08	−0.80	0.00	0.19	−0.37
2.75	0.19	0.03	−0.30	0.14	−0.30	−0.73	−0.37	0.31
3.41	0.16	−0.43	0.56	−0.23	0.17	0.05	−0.62	0.10
3.48	0.24	0.39	−0.29	−0.22	0.00	0.13	−0.49	−0.64
4.60	0.23	0.14	0.47	0.56	0.25	−0.37	0.14	−0.42
5.55	0.21	−0.46	−0.28	−0.43	0.41	−0.37	0.31	−0.26

$\varepsilon_1^a = \varepsilon_1 + t_p - t_1 - 2t_1' - 2t_2' - t_3$ of equation (40) is replaced by $\varepsilon_1^b = \varepsilon_1 - t_p + t_1' - 2t_2 - 2t_3$. In these equations, we have set

$$\varepsilon_0 = U - E_p - U_p - V + J \qquad \text{and} \qquad \varepsilon_0' = \varepsilon_0 + \tfrac{3}{2}J \tag{41}$$

$$\varepsilon_1 = \varepsilon_0 + V \qquad \text{and} \qquad \varepsilon_1' = \varepsilon_1 + \tfrac{3}{2}J \tag{42}$$

$$\gamma = \tfrac{1}{2}(t_1' + t_1'') \qquad \tau = \tfrac{1}{2}(t_2 + t_2') \tag{43}$$

and

$$t_1'' = \frac{t_0^2}{U - E_p - U_p - 3V} \qquad t_3 = \frac{t_0^2}{U - E_p - 2V}. \tag{44}$$

Note here that the nearest-neighbour attraction $-V$ is taken into account between extra charges on O $2p_{x,y}$ and Cu $3d_{x^2-y^2}$ orbitals in the basis states of $H_{I,I}$, but not for unbound basis states of $H_{II,II}$.

We know all material constants which are used in these expressions as shown in table 1 [26–30]. In terms of these constants, we have diagonalized the secular equations of A_{1g} and B_{1g} modes. The eigenenergies and eigenvectors are listed in tables 2 to 6 for La_2CuO_4, $Sr_2CuO_2Cl_2$, Nd_2CuO_4, Gd_2CuO_4 and $YBa_2Cu_3O_6$, respectively.

The eigenenergies of A_{2g} and B_{2g} modes are evaluated by using the eigenfunctions equations (20) and (21), respectively, within this approximation. They are found to be

Table 3. The eigenenergies and eigenvectors of A_{1g} and B_{1g} modes for $Sr_2CuO_2Cl_2$.

$E_i(A_{1g})$ (eV)	a_i	b_i	c_i	d_i	e_i	f_i	g_i	h_i
2.08	0.41	0.45	0.17	−0.25	0.30	0.32	0.39	0.43
2.41	0.07	−0.25	−0.42	0.53	0.48	0.46	−0.14	0.12
2.53	0.10	−0.35	0.22	−0.01	−0.35	0.61	0.41	−0.41
2.89	0.49	−0.25	−0.22	0.26	−0.54	−0.23	0.14	0.46
3.30	0.02	−0.55	0.63	−0.12	0.17	0.03	−0.33	0.38
3.55	0.54	0.14	−0.13	−0.29	−0.15	0.24	−0.67	−0.25
4.59	0.40	0.19	0.47	0.58	0.17	−0.28	0.02	−0.37
5.51	0.35	−0.44	−0.25	−0.39	0.43	−0.36	0.28	−0.28
$E_i(B_{1g})$ (eV)								
1.59	0.79	0.25	0.06	−0.11	0.09	0.29	0.26	0.37
2.36	0.10	0.07	0.37	−0.43	−0.70	−0.29	0.22	−0.19
2.42	0.31	−0.59	−0.21	0.40	−0.44	0.31	0.01	−0.24
2.59	0.27	0.01	−0.32	0.18	−0.19	−0.66	−0.42	0.37
3.30	0.10	−0.47	0.61	−0.21	0.18	0.07	−0.52	0.20
3.33	0.28	0.35	−0.19	−0.25	0.04	0.15	−0.57	−0.60
4.44	0.26	0.11	0.46	0.55	0.27	−0.38	0.15	−0.41
5.39	0.21	−0.47	−0.30	−0.45	0.41	−0.35	0.31	−0.24

Table 4. The eigenenergies and eigenvectors of A_{1g} and B_{1g} modes for Nd_2CuO_4.

$E_i(A_{1g})$ (eV)	a_i	b_i	c_i	d_i	e_i	f_i	g_i	h_i
1.78	0.43	0.36	0.07	−0.09	0.42	0.43	0.35	0.43
2.40	0.10	0.19	0.47	−0.52	−0.53	−0.12	0.39	−0.12
2.55	0.05	−0.45	0.03	0.21	−0.17	0.69	0.30	−0.40
2.83	0.55	−0.31	−0.21	0.25	−0.51	−0.17	−0.00	0.46
3.26	0.02	0.52	−0.66	0.16	−0.21	−0.07	0.34	−0.32
3.44	0.48	0.18	−0.10	−0.33	−0.10	0.27	−0.66	−0.32
4.47	0.41	0.17	0.46	0.56	0.18	−0.30	0.03	−0.39
5.36	0.33	−0.45	−0.27	−0.41	0.41	−0.35	0.28	−0.27
$E_i(B_{1g})$ (eV)								
1.45	0.71	0.27	0.04	0.07	0.22	0.36	0.27	0.40
2.36	0.27	−0.02	0.34	−0.37	−0.74	−0.20	0.23	−0.15
2.50	0.43	−0.54	−0.35	0.47	−0.33	0.11	−0.25	−0.02
2.56	0.18	0.25	−0.16	−0.05	−0.02	−0.72	−0.40	0.45
3.26	0.04	0.55	−0.65	0.11	−0.18	−0.04	0.25	−0.40
3.30	0.28	0.17	0.08	−0.35	0.13	0.22	−0.69	−0.48
4.35	0.28	0.11	0.45	0.54	0.27	−0.38	0.13	−0.42
5.30	0.22	−0.47	−0.30	−0.46	0.41	−0.34	0.30	−0.24

degenerate and

$$E_{a'} = E_{b'} = U - E_p - U_p - V + \tfrac{5}{2}J. \tag{45}$$

When we use the material constants in table 1, these eigenenergies are numerically obtained to be larger than 3.0 eV as shown in table 7.

These eigenenergies of A_{1g} and B_{1g} modes are plotted in figure 4 showing the absorption spectrum together with the dipole-allowed E_u modes. Two crystals Nd_2CuO_4 and Gd_2CuO_4 have very similar material constants and consequently similar spectrum structures. Therefore the spectrum of E_u, A_{1g} and B_{1g} has been drawn only for Nd_2CuO_4 in figure 4.

Table 5. The eigenenergies and eigenvectors of A_{1g} and B_{1g} modes for Gd_2CuO_4.

$E_i(A_{1g})$ (eV)	a_i	b_i	c_i	d_i	e_i	f_i	g_i	h_i
1.83	0.43	0.36	0.07	−0.09	0.42	0.43	0.35	0.43
2.43	0.10	0.19	0.47	−0.52	−0.53	−0.13	0.39	−0.12
2.58	0.05	−0.44	0.04	0.20	−0.18	0.69	0.30	−0.40
2.86	0.54	−0.30	−0.22	0.26	−0.51	−0.17	0.01	0.46
3.29	0.01	0.53	−0.66	0.15	−0.20	−0.06	0.34	−0.33
3.47	0.48	0.18	−0.10	−0.32	−0.10	0.27	−0.66	−0.32
4.50	0.41	0.17	0.46	0.53	0.18	−0.30	0.04	−0.39
5.38	0.33	−0.45	−0.27	−0.41	0.41	−0.35	0.28	−0.27
B_{1g}								
1.50	0.71	0.27	0.04	−0.07	0.22	0.36	0.27	0.40
2.40	0.28	−0.02	0.34	−0.36	−0.75	−0.21	0.23	−0.15
2.53	0.42	−0.55	−0.35	0.47	−0.32	0.13	−0.24	−0.03
2.59	0.19	0.23	−0.18	−0.03	−0.02	−0.71	−0.41	0.45
3.29	0.04	0.55	0.65	0.12	−0.19	−0.04	0.27	−0.39
3.32	0.28	0.18	0.07	−0.34	0.13	0.22	−0.68	0.49
4.37	0.28	0.11	0.45	0.54	0.27	−0.38	0.14	−0.42
5.30	0.21	−0.47	−0.30	−0.46	0.41	−0.34	0.30	−0.24

Table 6. The eigenenergies and eigenvectors of A_{1g} and B_{1g} modes for $YBa_2Cu_3O_6$.

$E_i(A_{1g})$ (eV)	a_i	b_i	c_i	d_i	e_i	f_i	g_i	h_i
2.03	0.20	0.56	0.27	−0.41	0.26	0.09	0.37	0.44
2.24	0.10	−0.20	−0.12	0.27	0.38	0.82	0.22	−0.04
2.38	0.03	−0.11	0.38	−0.30	−0.16	0.05	0.13	0.07
3.07	0.25	−0.24	−0.22	0.34	−0.44	−0.13	0.46	0.54
3.56	0.01	−0.58	0.64	−0.12	0.09	0.04	−0.27	0.40
4.38	0.52	0.10	−0.26	−0.30	−0.37	0.34	−0.54	0.13
5.73	0.52	0.30	0.46	0.60	0.00	−0.10	−0.12	−0.13
6.94	0.60	−0.38	−0.18	−0.30	0.38	−0.34	0.21	−0.28
$E_i(B_{1g})$ (eV)								
1.24	0.79	0.25	0.07	−0.13	0.03	0.27	0.28	0.37
2.12	0.14	−0.05	0.23	−0.26	−0.82	−0.33	0.17	−0.22
2.20	0.19	−0.54	−0.17	0.38	−0.16	0.05	0.13	0.07
2.48	0.31	−0.19	−0.43	0.40	−0.17	−0.47	−0.40	0.34
3.44	0.33	0.08	0.13	−0.30	0.10	0.11	−0.76	−0.42
3.55	0.03	0.60	−0.63	0.08	−0.07	−0.01	0.17	−0.44
5.14	0.27	0.05	0.44	0.50	0.32	−0.40	0.21	−0.41
6.44	0.19	−0.49	−0.34	−0.51	0.37	−0.31	0.28	−0.20

Table 7. The lowest levels of A_{2g} and B_{2g} modes ($E(A_{2g}) = E(B_{2g})$).

	La_2CuO_4	$Sr_2CuO_2Cl_2$	Nd_2CuO_4	Gd_2CuO_4	$YBa_2CuO_3O_6$
$E_i(A_{2g})$ (eV)	3.35	3.24	3.23	3.15	3.35

4. Large-shift Raman and two-photon absorption

The large-shift RS, e.g. due to the CT excitations of A_{1g}, B_{1g}, A_{2g} and B_{2g} modes, is the second-order nonlinear optical processes. The incident radiation field with angular frequency

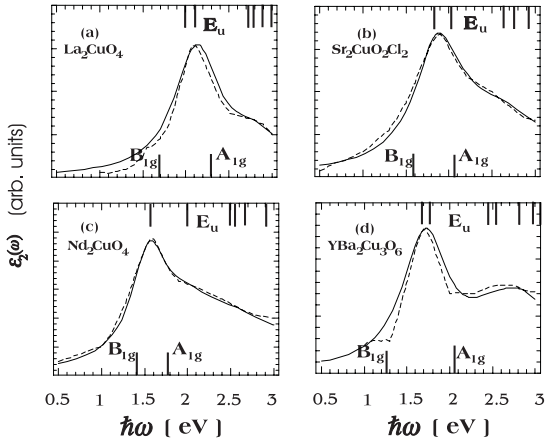

Figure 4. Experimental and theoretical absorption spectra $\varepsilon_2(\omega)$ of (a) La_2CuO_4 [3]; (b) $Sr_2CuO_2Cl_2$ [3]; (c) Nd_2CuO_4 [3]; and (d) $YBa_2Cu_3O_6$ [7]. The full curve is the theoretical $\varepsilon_2(\omega)$ with the use of $\Gamma_{1,2} = 0.32$ eV, $\Gamma_{i\geqslant 3} = 0.34$ eV (La_2CuO_4), $\Gamma_{1,2} = 0.32$ eV, $\Gamma_{i\geqslant 3} = 0.36$ eV ($YBa_2Cu_3O_6$) and $\Gamma_1 = 0.25$ eV, $\Gamma_{i\geqslant 2} = 0.44$ eV (Nd_2CuO_4), $\Gamma_1 = 0.28$ eV, $\Gamma_{i\geqslant 2} = 0.48$ eV ($Sr_2CuO_2Cl_2$) and the broken curve is the experimental $\varepsilon_2(\omega)$. On the bottom lines, the calculated even-parity modes are drawn in agreement with the observed values for (a), (b), (c) and (d) with modified assignments.

$\omega_i \equiv \omega$ much larger than the lowest excitation energies $E_1(A_{1g})$, $E_1(B_{1g})$, $E(A_{2g})$ and $E_1(B_{2g})$ is scattered into the radiation field with the scattered frequency $\omega_s = \omega - E(X)$ ($X = A_{1g}$, B_{1g}, A_{2g} and B_{2g}). The scattering intensity is described by the absolute square of the Raman tensor:

$$\chi^{fg}_{\alpha\beta}(\omega) = \sum_{i\neq g,f} \left\{ \frac{P^{\alpha}_{fi} P^{\beta}_{ig}}{E_{ig} - \omega - \mathrm{i}\Gamma_i} + \frac{P^{\beta}_{fi} P^{\alpha}_{ig}}{E_{if} + \omega + \mathrm{i}\Gamma_i} \right\}. \tag{46}$$

Here $\boldsymbol{P}$ denotes the crystal transition dipole moment operator and (α, β) mean the polarization directions of the scattered and incident radiation field, respectively. In the case of the large-shift RS, the energy difference between the final (f) and the ground (g) states of the crystal $E_{fg} = E_f - E_g$ is equal to the lowest excitation energy of Raman-active modes $E_1(X)$ ($X = A_{1g}$, B_{1g}, A_{2g} and B_{2g}).

The two-photon absorption (TPA) spectrum is also expressed as the square of the following TPA tensor:

$$\chi^{fg}_{\alpha\beta}(\omega_1, \omega_2) = \sum_{i\neq g,f} \left\{ \frac{P^{\alpha}_{fi} P^{\beta}_{ig}}{E_{ig} - \omega_1} + \frac{P^{\beta}_{fi} P^{\alpha}_{ig}}{E_{ig} - \omega_2} \right\}. \tag{47}$$

The TPA spectrum shows the peak when the sum of two photon energies $\omega_1 + \omega_2$ becomes equal to the two-photon allowed excitations $E_{fg} = E_f - E_g = E(X)$ ($X = A_{1g}$, B_{1g}, A_{2g} or B_{2g}). The intermediate states $|i\rangle$ consist of the dipole-allowed states with E_u representation of D_{4h} symmetry. In the present paper, we discuss the polarization dependence of both large-shift RS and TPA. Let us represent the polarization P^{β} of incident light ω_i (the first photon ω_1 in the case of TPA) by the polarization vector $\widehat{\epsilon}_1 = (l_1, m_1, n_1)$ and that P^{α} of the scattered light ω_s (the second photon ω_2 in the case of TPA) by $\widehat{\epsilon}_2 = (l_2, m_2, n_2)$.

Both large-shift RS and TPA of the insulating cuprates have been observed usually by using the surface perpendicular to the z-axis. For example, almost all large-shift RS were observed under the following configurations, $z(xx)\bar{z}$, $z(xy)\bar{z}$, $z(x'x')\bar{z}$, $z(x'y')\bar{z}$ [20, 21]. Here

Table 8. Selection rules of RS for D_{4h} and $D_{2h}(C_{2h})$ point groups. [A]: $\chi_{xx}(A_1) = \chi_{yy}(A_1) = p$, $\chi_{xx}(B_1) = -\chi_{yy}(B_1) = q$, $\chi_{xy}(A_2) = -\chi_{yx}(A_2) = -r$, $\chi_{xy}(B_2) = \chi_{yx}(B_2) = s$, $\chi_{x'x'}(A_1) = \chi_{y'y'}(A_1) = p$, $\chi_{x'x'}(B_2) = -\chi_{y'y'}(B_2) = s$, $\chi_{x'y'}(B_1) = \chi_{y'x'}(B_1) = -q$, $\chi_{x'y'}(A_2) = -\chi_{y'x'}(A_2) = r$. [B]: $\chi_{xx}(a) = \chi_{yy}(a) = p$, $\chi_{xx}(b) = -\chi_{yy}(b) = q$, $\chi_{xy}(a) = \chi_{yx}(a) = s$, $\chi_{xy}(b) = -\chi_{yx}(b) = -r$.

	$z(xx)\bar{z}$	$z(xy)\bar{z}$	$z(x'x')\bar{z}$	$z(x'y')\bar{z}$	$z(x \pm iy, x \pm iy)\bar{z}$	$z(x \pm iy, x \mp iy)\bar{z}$
[A]: D_{4h}: $x' \parallel [110]$, $y' \parallel [\bar{1}10]$						
A_{1g}	p		p		p	
B_{1g}	q			$-q$		q
A_{2g}		r		$-r$	$\pm ir$	
B_{2g}		s	s			$\mp is$
[B]: $D_{2h}(C_{2h})$: $x' \parallel [110]$, $y' \parallel [\bar{1}10]$, sublattice magnetization $\parallel x'$						
A_g	p	s	$p+s$		p	$\mp is$
$B_{1g}(B_g)$	q	r		$-q-r$	$\pm ir$	q

polarization geometries are described using the Porte notation $i(jk)l$, where i and l represent the propagation directions, and j and k the polarization directions of the incident and scattered light, respectively [35]. We confine ourselves to the configuration of two incident light rays propagating in the z-direction in both large-shift RS and TPA for simplicity. Then the polarization dependence of RS (TPA) is described in terms of the polarization angles θ_1 and θ_2 measured from the x-axis for the incident (or the first photon) and the scattered (or the second photon) light rays, respectively, as follows [36, 37]:

$$A_{1g} : p \times \cos(\theta_1 - \theta_2) \tag{48}$$

$$B_{1g} : q \times \cos(\theta_1 + \theta_2) \tag{49}$$

$$A_{2g} : r \times \sin(\theta_2 - \theta_1) \tag{50}$$

$$B_{2g} : s \times \sin(\theta_1 + \theta_2). \tag{51}$$

See also the table 8 for Raman tensors. The magnitude, for example, of the value p is estimated by considering the microscopic mechanism. As long as we choose for the states $|g\rangle$, $|i\rangle$ and $|f\rangle$ the levels among the states arising from the CT between the $O(2p_\sigma)$ and $Cu(3d_{x^2-y^2})$ orbitals, both Raman and TPA tensors vanish. When we choose the O(3s) level as the intermediate state $|i\rangle$, $p \equiv \chi_{xx}[A_{1g}]$ for the large-shift RS per unit cell is evaluated as

$$\chi_{xx}[A_{1g}] = \sum_j \frac{\langle A_{1g}|P^x|\mathrm{O\ 3s}(j)\rangle\langle \mathrm{O\ 3s}(j)|P^x|g\rangle}{E_{3s} - E_{2p} - U_p - \omega} \tag{52}$$

$$= \frac{a_1[A_{1g}]\mu'_x\mu''_x}{E_{3s} - E_{2p} - U_p - \omega}. \tag{53}$$

Here we have introduced the intra-atomic transition dipole moment $\mu'_x \equiv \langle \mathrm{O\ 3s}|P^x|\mathrm{O\ 2p}_x\rangle$ and the CT dipole moment $\mu''_x \equiv \langle \mathrm{Cu\ 3d}_{x^2-y^2}|P^x|\mathrm{O\ 3s}\rangle$ between the nearest neighbours on the x-axis. The expansion coefficient $a_1[B_{1g}]$ of the term Ψ^1_{a+} in equation (34) is nearly equal to one for the lowest B_{1g} state while $a_1[A_{1g}]$ is much smaller than one as tables 2–6 show. In this approximation, $|\chi_{xx}[B_{1g}]| \equiv |q| > |\chi_{xx}[A_{1g}]| \equiv |p|$. For the TPA tensor, the same process may be considered to be relevant but the single photon $\omega_1 \approx \omega_2$ is in the region of infrared so that the energy denominator of equation (53) becomes a little larger than in the case of large-shift RS.

5. Discussion

The absorption spectrum was found to be sensitive to the CT values of t_0 and t_p as well as the exciton binding energy V. The material constants are listed in table 1. These values have been fixed for materials so as to obtain the best agreement between the observed and calculated absorption spectra as shown in figure 4. First, we note that the values as well as the signs of t_0 and t_p are also in good agreement with the first-principles calculations except for T'-phase Nd_2CuO_4 and Gd_2CuO_4. In the exceptional case, for example, our optimum value of t_p is 0.3 eV while the first-principles value is 0.39 eV for Nd_2CuO_4 [31]. This discrepancy will be removed by estimating the presence and absence of the contribution from apical oxygens [38, 39] to t_p through the indirect channel via the $2p_z$ orbital of the apical oxygens for the T-phase perovskite La_2CuO_4 and the T'-phase Nd_2CuO_4, respectively. When we subtract this contribution from the value t_p of the T-phase for the case of the T'-phase without the apical oxygens, we have the t_p values which have been obtained as shown in table 1 by fitting the absorption spectrum. Here the transfer matrix element and the energy difference between the $O(2p_\sigma)$ orbital on the CuO_2 plane and the apical $O(2p_z)$ were assumed to be 0.3 eV and 2.0 eV, respectively. Second, we could also describe the enhancement spectra of two-magnon RS for La_2CuO_4 and $YBa_2Cu_3O_6$ with agreement between the theory and the experiment in terms of the material constants determined above [32]. In the present paper, we have evaluated in terms of these material constants the eigenenergies of even-symmetry modes which are observable in large-shift RS and TPA spectra.

We compare our calculated eigenenergies of B_{1g} and A_{1g} modes with the observed large-shift RS signals. Two strong signals were observed below and around 2 eV but their polarization dependence is not so clear [21]. Two peak energies are found to agree very well with the calculated eigenenergies of B_{1g} and A_{1g} modes. As we can imagine from the lowest-order calculation given in (5), $E(B_{1g}) = E_0 - t_1 - t_p$ and $E(A_{1g}) = E_0 + 3t_1 + 2t_p$ with both positive t_1 and t_p, we believe that the lower and higher energy signals correspond, respectively, to the B_{1g} and A_{1g} modes. However, the assignments of [21] look inconsistent. For example, the lower (11 900 cm^{-1}) and higher (13 000 cm^{-1}) signals were assigned, respectively, to B_{1g} and A_{1g} modes for Gd_2CuO_4, while the assignment was reversed for $YBa_2Cu_3O_6$. Furthermore, they claimed that there seemed to be no A_{1g} and B_{1g} Raman features present for La_2CuO_4. The signal at 12 000 cm^{-1} of Gd_2CuO_4 was assigned to the A_{2g} mode.

Let us discuss this discrepancy. It is well known for La_2CuO_4 [10] that the paramagnetic tetragonal phase shows D_{4h} symmetry above 515 K and the orthorhombic phase with D_{2h} is realized below 515 K. All crystals except $Sr_2CuO_2Cl_2$ show this phase transition of the crystal structures. Strictly speaking the point group D_{4h} should not be applied to the AF orthorhombic phase as the π-rotations C_2' and C_2'' of D_{4h} around the axes perpendicular to the principal axis C change the sign of the components of the sublattice magnetization vector in the a–b plane [40, 41]. We consider both the crystals to have D_{2h} symmetry with [110], [$\bar{1}$10] and [001], i.e. x'-, y'- and z-axes, as their three two-fold axes even in the AF phase as long as the sublattice magnetization orients in the [110] direction. This is because the unitary part of the magnetic group $G_0 = \{E_i, C_{2x'}, C_{2y'}(\tau), C_2(\tau)\} = C_{2h} + C_2(\tau)C_{2h}$ with $C_{2h} = \{E, C_{2x'}\}$ is isomorphic to the group $D_{2h} = \{E, C_{2x}, C_{2y}, C_2\}$, where τ is the shortest vector connecting two Cu ions in the A- and B-sublattices.

We summarize the selection rules of large-shift RS for D_{4h} and $D_{2h}(C_{2h})$ point groups in table 8. Four Raman-active modes of D_{4h} are merged into two modes of $D_{2h}(C_{2h})$ as

$$\begin{aligned} A_{1g}, B_{2g} &\longrightarrow A_g(D_{2h}) \\ &\longrightarrow A_g(C_{2h}) \end{aligned} \tag{54}$$

$$B_{1g}, A_{2g} \longrightarrow B_{1g}(\mathrm{D}_{2h}) \longrightarrow B_g(\mathrm{C}_{2h}). \tag{55}$$

Therefore it is interesting to observe how different two RS intensities are between the configuration $z(x'x')\bar{z}$ and $z(y', y')\bar{z}$ or/and between $z(x', y')\bar{z}$ and $z(y', x')\bar{z}$. The difference in the first case is induced because the x'-axis [110] is not equivalent to the y'-axis [$\bar{1}$10] in the symmetry $\mathrm{D}_{2h}(\mathrm{C}_{2h})$, i.e. $|\chi_{x'x'}(a)|^2 = |p+s|^2$ and $|\chi_{y'y'}(a)|^2 = |p-s|^2$ as table 8 shows. For the second case, $|\chi_{x'y'}(b)|^2 = |q+r|^2$ and $|\chi_{y'x'}(b)|^2 = |q-r|^2$. The observations of these differences will support the D_{2h} or C_{2h} symmetry rather than D_{4h} in the AF phase. Note also that these differences originate in the $B_{2g}(s)$ and $A_{2g}(r)$ modes of the D_{4h} representation.

The present CT model predicts the eigenenergies of A_{2g} and B_{2g} in D_{4h} symmetry at an energy of more than 3 eV as described in table 7. However, the intra-atomic transition from $\mathrm{Cu}(3\mathrm{d}_{xy})$ to $\mathrm{Cu}(3\mathrm{d}_{x^2-y^2})$ has the excitation energy 1.4 eV for the metallic $YBa_2Cu_3O_7$ [7]. Therefore we may expect the mixing of this intra-atomic transition with the CT excitation of the B_{1g} mode due to (55) through the lower-symmetry crystalline field of $\mathrm{D}_{2h}(\mathrm{C}_{2h})$ because those excitation energies are close to each other. When we observe that $|s| \ll |p|$ at $E(A_{1g})$ and $|r| \ll |q|$ at $E(B_{1g})$, the present CT model under D_{4h} symmetry is well justified. When $|r| \simeq |q|$, the lower-symmetry crystalline field D_{2h} should be taken into account as the perturbation on the eigenstates of the D_{4h} representation.

Two-photon absorption intensity should also obey the same polarization dependence given by (48)–(51). We may expect the lower-symmetry crystalline field to be weak enough so that this will be treated as the perturbations on the eigenstates obtained under the D_{4h} point group. We believe that the present model under D_{4h} symmetry will give us a good starting point to describe nonlinear optical responses of the insulating cuprates.

The tetragonal structure remains for $Sr_2CuO_2Cl_2$ until low temperatures without suffering the crystalline structure change into the orthorhombic phase. Therefore the description of eigenstates based upon D_{4h} symmetry will work correctly, in contrast to other crystals which exhibit structural change into an orthorhombic phase. Observation of the large-shift RS for this crystal has not been attempted yet. Therefore the observation of the polarization dependence both of two-photon absorption and large-shift RS in this crystal will be able to establish the validity of the present theory. The precise measurements of the polarization dependence for Nd_2CuO_4, Gd_2CuO_4, La_2CuO_4 and $YBa_2Cu_3O_6$ will give us further confirmation of the present theory and information on how well these crystals may be described by D_{4h} or $\mathrm{D}_{2h}(\mathrm{C}_{2h})$ symmetry.

The calculated hole band widths $8t_p = 4.0$ eV (La_2CuO_4) and 4.4 eV ($YBa_2Cu_3O_6$) are close to the observed ones. On the other hand, the exciton band width is estimated as $2t_p[t_0/(E_p + U_p)]^2 = 10$ meV and 40 meV for La_2CuO_4 and $YBa_2Cu_3O_6$, respectively. Deriving the dispersion relation of the bound as well as unbound electron–hole pair in the present model is also a future problem.

Acknowledgments

EH thanks Professor M V Klein, Professor Y Tokura and Professor S Uchida for fruitful discussions and important information relevant to the present calculations.

References

[1] Imada M, Fujimori A and Tokura Y 1998 *Rev. Mod. Phys.* **70** 1039
[2] Tokura Y (ed) 2000 *Colossal Magnetoresistive Oxides* (London: Gordon and Breach)

[3] Tokura Y, Koshihara S, Arima T, Takagi H, Ishibashi S, Ido T and Uchida S 1990 *Phys. Rev.* B **41** R11 657
[4] Arima T, Kikuchi K, Kasuya M, Koshihara S, Tokura Y, Ido T and Uchida S 1991 *Phys. Rev.* B **44** R917
[5] Tio T, Birgeneau R J, Cassanko A and Kasten M A 1990 *Phys. Rev.* B **42** R10 800
[6] Falck J P, Levy A, Kastner M A and Birgeneau R J 1992 *Phys. Rev. Lett.* **69** 1109
[7] Romberg H, Nücker N, Fink J, Wolf Th, Xi X X, Koch B, Geserich H P, Dürrler M, Assmus W and Gegenheimer B 1990 *Z. Phys.* B **78** 367
[8] Cooper S L, Thomas G A, Millis A J, Sulewski P E, Orenstein J, Rapkine D H, Cheong S-W and Trevor P L 1990 *Phys. Rev.* B **42** R10 785
[9] Cooper S L, Reznik D, Kotz A, Karlov M A, Liu R, Klein M V, Veal B W and Paulikas A P 1993 *Phys. Rev.* B **47** 8233
[10] Sugai S 1989 *Phys. Rev.* B **39** 4306
[11] Heyen E T, Kircher J and Cardona M 1992 *Phys. Rev.* B **45** 3037
[12] Lyons K B, Fleury P A, Schneemeyer L F and Waszczak J V 1988 *Phys. Rev. Lett.* **60** 732
[13] Lyons K B, Fleury P A, Remeika J P, Cooper A S and Negran T J 1988 *Phys. Rev.* B **37** 2353
[14] Lyons K B, Sulewski P E, Fleury P A, Carter H L, Cooper A S, Espinosa G P, Fish Z and Cheong S-W 1989 *Phys. Rev.* B **39** R9693
[15] Sugai S, Shamoto S and Sato M 1988 *Phys. Rev.* **38** 6436
[16] Yoshida M, Tajima S, Koshizuka N, Tanaka S, Uchida S and Itoh T 1992 *Phys. Rev.* B **46** 6505
[17] Liu R, Klein M V, Salamon D, Cooper S L, Lee W C, Cheng S-W and Ginsberg D M 1993 *J. Phys. Chem. Solids* **54** 1347
[18] Knoll P, Mayer M, Brenig W and Waidacher Ch 1996 *J. Low Temp. Phys.* **105** 383
[19] Blumberg G, Abbamonte P, Klein M V, Lee W C, Ginsberg D M, Miller L L and Zibold A 1996 *Phys. Rev.* B **53** R11 930
[20] Liu R, Salamon D, Klein M V, Cooper S L, Lee W C, Cheng S-W and Ginsberg D M 1993 *Phys. Rev. Lett.* **71** 3709
[21] Salamon D, Liu R, Klein M V, Karlow M V, Cooper S L, Cheng S-W, Lee W C and Ginsberg D M 1995 *Phys. Rev.* B **51** 6617
[22] Wells B O, Shen Z-X, Matsuura A, King D M, Kastner M A, Greven M and Birgeneau R J 1995 *Phys. Rev. Lett.* **74** 964
[23] Wang Y Y, Zhang F C, Dravid V P, Ng K K, Klein M V, Schnatterly S E and Miller L L 1996 *Phys. Rev. Lett.* **77** 1809
[24] Pothuizen J J M, Eder R, Hien N T, Matoba M, Menovsky A A and Sawatzky G A 1997 *Phys. Rev. Lett.* **78** 717
[25] Kuiper P, Guo J H, Sathe C, Duda L C and Nordgren J 1998 *Phys. Rev. Lett.* **80** 5204
[26] Hanamura E, Dan N T and Tanabe Y 2000 *J. Phys.: Condens. Matter* **12** L345
[27] Herman F, Kasowski R V and Hsu V Y 1987 *Phys. Rev.* B **36** 6904
[28] McMahan A K, Martin R M and Satpathy S 1988 *Phys. Rev.* B **38** 6650
[29] Mattheiss L F and Hamann D R 1989 *Phys. Rev.* B **40** 2217
[30] Eskes H, Tjeng L H and Sawatzky G A 1990 *Phys. Rev.* B **41** 288
[31] Mizuno Y, Tokyama Y and Maekawa S 1998 *Phys. Rev.* **58** R14 713
[32] Hanamura E, Dan N T and Tanabe Y 2000 *Phys. Rev.* B **62** 7003
[33] Keimer B *et al* 1992 *Phys. Rev.* B **46** 14 034
[34] Inui T, Tanabe Y and Onodera Y 1990 *Group Theory and Its Applications in Physics (Springer Series in Solid-State Sciences vol 78)* (Berlin: Springer)
[35] Shastry B S and Shraimen B I 1990 *Phys. Rev. Lett.* **65** 1068
Shastry B S and Shraimen B I 1991 *Int. J. Mod. Phys.* B **5** 365
[36] Inoue M and Toyozawa Y 1965 *J. Phys. Soc. Japan* **20** 363
[37] Bader T R and Gold A 1968 *Phys. Rev.* **171** 997
[38] Matsukawa H and Fukuyama H 1990 *J. Phys. Soc. Japan* **59** 1723
Matsukawa H and Fukuyama H 1989 *J. Phys. Soc. Japan* **58** 3687
Matsukawa H and Fukuyama H 1989 *J. Phys. Soc. Japan* **58** 2845
[39] Fukuyama H, Matsukawa H and Hasegawa Y 1989 *J. Phys. Soc. Japan* **58** 364
[40] Dimmock J O and Wheeler R G 1962 *Phys. Rev.* **127** 391
[41] Birss R R 1964 Symmetry and magnetism *Selected Topics in Solid State Physics* vol III, ed E P Wohlfarth (Amsterdam: North-Holland)